

SN 2020jgb

AUTHORS¹

¹*Center for Interdisciplinary Exploration and Research in Astrophysics (CIERA), Department of Physics and Astronomy, Northwestern University, 1800 Sherman Road, Evanston, IL 60201, USA*

ABSTRACT

Keywords: keywords

1. INTRODUCTION

- Thin shell (shell mass $\lesssim 0.03 M_{\odot}$), usually normal-luminosity
 - SN 2016jhr (Jiang et al. 2017) - thin shell, near- M_{Ch} ($1.38 M_{\odot} + 0.01 M_{\odot}$)
 - SN 2018aoz ($1.05 M_{\odot} + 0.01 M_{\odot}$) (Ni et al. 2022)
- Thick shell (shell mass $> 0.03 M_{\odot}$), usually sub-luminous (18byg-like)
 - SN 2018byg ($0.76 M_{\odot} + 0.15 M_{\odot}$) (De et al. 2019)
- Ambiguous (Ca-rich Ia)
 - subluminous, line-blanketing in the photometric phase, strong [Ca II] emission in the nebular phase, but also some 91bg-like features
 - SN 2016hmk as a He-shell double detonation (DDet) (Jacobson-Galán et al. 2020) ($0.85 M_{\odot} + 0.02 M_{\odot}$) or a near-Chandrasekhar mass, 91bg-like object (Galbany et al. 2019)
 - SN 2019ofm (De et al. 2020)
- (Polin et al. 2019), historical papers by Woosley, Boyle+ (2019)

2. OBSERVATIONS

2.1. Discovery

SN 2020jgb was first discovered by the Zwicky Transient Facility (ZTF; Bellm et al. 2019; Graham et al. 2019) on 2020 May 03.463 UT (MJD 58972.463) with the 48-inch Samuel Oschin Telescope (P48) at Palomar Observatory. The automated ZTF discovery pipeline (Masci et al. 2019) detected SN 2020jgb using the image-differencing technique of Zackay et al. (2016). The candidate passed internal thresholds (e.g., Mahabal et al.

2019; Duev et al. 2019), leading to the production and dissemination of a real-time alert (Patterson et al. 2019) and the internal designation ZTF20aayhacx. It was detected at a magnitude of 19.86 in the g_{ZTF} -band, and J2000 coordinates $\alpha = 17^{\text{h}}53^{\text{m}}12^{\text{s}}.651$, $\delta = -00^{\circ}51'21''.81$ and announced to the public in Fremling (2020). The last non-detection was on 2020 April 27.477 (MJD 58966.477; 5.99 days before the first detection) up to a limiting magnitude of 20.7 in the r_{ZTF} -band. This transient was identified as a SN Ia by Dahiwalé & Fremling (2020) due to the prominent Si II absorption features and a lack of any H features in the spectrum obtained on 2020 May 28.468.

2.2. Optical Photometry

SN 2020jgb was monitored in the g_{ZTF} and r_{ZTF} -bands by ZTF as part of its ongoing Northern Sky Survey (Bellm et al. 2019). We adopt a Galactic extinction of $E(B - V) = 0.404 \text{ mag}$ (Schlafly & Finkbeiner 2011), and correct all photometry using the Fitzpatrick (1999) extinction model. We assume there is no additional extinction in the host galaxy. This assumption is supported by the lack of Na I D absorption at the redshift of the host galaxy, though see Poznanski et al. (2011) for caveats on the use of Na I D absorption as a proxy for extinction.

To get the distance modulus to SN 2020jgb, we use the 2M++ model (Carrick et al. 2015) to obtain a peculiar velocity towards its host galaxy, PSO J175312.663+005122.078, to be 181 km s^{-1} . This, combined with the recession velocity in the frame of the cosmic microwave background¹ (CMB) $v_{\text{CMB}} = 8997 \text{ km s}^{-1}$, give a net Hubble recession velocity is 9170 km s^{-1} [AAM: uncertainty?]. Adopting $H_0 = 70 \text{ km s}^{-1} \text{ Mpc}^{-1}$, we estimate the luminosity distance

¹ See https://ned.ipac.caltech.edu/velocity_calculator.

Table 1. Spectroscopic Observations of SN 2020jgb and the host galaxy.

t_{obs}	Phase	Telescope/	R	Range	Air
(MJD)	(d)	Instrument	($\lambda/\Delta\lambda$)	(\AA)	Mass
58,976.42	−9.7	P60/SEDm	100	3770–9220	1.23
58,982.12	−4.2	NOT/ALFOSC	360	4000–9620	1.17
58,990.43	+3.9	P60/SEDm	100	3770–9220	1.23
58,997.44	+10.7	P60/SEDm	100	3770–9220	1.29
58,998.41	+11.6	Shane/Kast	750	3620–10720	1.28
59,008.41	+21.3	P60/SEDm	100	3770–9220	1.28
59,009.45	+22.4	Gemini-N/GNIRS	1800	8230–25150	1.07
59,010.40	+23.3	P200/DBSP	700	3200–9500	1.27
59,023.58	+36.1	Keck I/LRIS	1100	3200–10250	2.04
59,107.29	+117.3	Keck I/LRIS	1100	3200–10250	1.31
59,143.26	+152.2	Keck I/LRIS	1100	3200–10250	2.16
59,669.60	host	Keck II/DEIMOS	2100	4500–8700	1.14

NOTE—Phase is measured relative to the r_{ZTF} -band peak in the host galaxy rest frame. The resolution R is reported for the central region of the spectrum.

to SN 2020jgb to be 134.1 Mpc, which yields a distance modulus of $\mu = 35.64$.

The forced photometry light curves (absolute magnitudes) in g_{ZTF} - and r_{ZTF} -bands are shown in Figure 1, in which we show all the measurements with $\text{SNR} > 2$.

2.3. Optical Spectroscopy

We obtained optical spectroscopic follow-up of the object from ~ -10 days to $\sim +150$ days relative to the r_{ZTF} -band peak, using the Spectral Energy Distribution Machine (SEDm; Blagorodnova et al. 2018) on the automated 60 inch telescope (P60; Cenko et al. 2006) at Palomar Observatory, the Kast Double Spectrograph (Miller & Stone 1994) at the Shane 3 m Telescope, the Andaluia Faint Object Spectrograph and Camera (ALFOSC)² installed at the Nordic Optical Telescope (NOT), the Double Beam Spectrograph (DBSP) on the 200 inch Hale telescope (P200; Oke & Gunn 1982), the Low Resolution Imaging Spectrograph (LRIS) on the Keck I telescope (Oke et al. 1995). Spectra were reduced using standard procedures (e.g., Matheson et al. 2000). Details of the spectroscopic observations are listed in Table 1, and the spectral sequence is shown in Figure 2.

On 2022 March 31, two years after the transient faded, we also took a spectrum for its host galaxy using the DEep Imaging Multi-Object Spectrograph (DEIMOS) on the Keck II telescope (Faber et al. 2003), for a total integration time of 3200 s. The spectra were reduced

with the PyPeIt Python package (Prochaska et al. 2020).

2.4. Near-infrared (NIR) Spectroscopy

We obtained one NIR (0.8–2.5 μm) spectrum of SN 2020jgb using the Gemini near-infrared spectrometer (GNIRS; Elias et al. 1998) on the Gemini North telescope on 2020 June 9 (~ 22 days after r_{ZTF} -band peak), for an integration time of 2400 s. The GNIRS spectrum was reduced with the PyPeIt package.

3. ANALYSIS

3.1. Photometric Properties

SN 2020jgb exhibited a fainter light curve than normal SNe Ia. In Figure 1, we compare the photometric properties of SN 2020jgb with the nearby, well-observed SN 2011fe (Nugent et al. 2011) and two Hershell DDet candidates, SN 2016jhr (Jiang et al. 2017) and SN 2018byg (De et al. 2019), with available photometric data on the Open Supernova Catalog³ (Guillochon et al. 2017).

The first detection was made on MJD=58972.46 in the g_{ZTF} -band. At a similar phase relative to the peak light, the luminosity was similar to the canonical object SN 2011fe and also the two DDet candidates. But within the ~ 10 days before peak luminosity, . Near peak, the DDet sample is heterogeneous in luminosity. And the decline rates also show diversity in both bands.

In the right panel of Figure 1, we also compare the color evolution ($g-r$) of these objects as measured from their first light t_{H} , accompanied by 62 normal SNe Ia (open circles) observed within 5 days of t_{H} by ZTF (from Bulla et al. 2020). For SN 2020jgb the early rise of the light curve was not well sampled, so we take the midpoint of the first detection and the last non-detection as an approximation of the first light time t_{H} , with the uncertainty (≈ 3 days) being half of the offset between these two epochs. We also estimate the $1-\sigma$ uncertainty of the $g_{\text{ZTF}} - r_{\text{ZTF}}$ color (the shaded region) in SN 2020jgb by fitting the forced photometry light curves in individual bands with Gaussian process (GP). The GP regression is conducted with the `gaussian_process` module in the `scikit-learn` package (Pedregosa et al. 2011), in which a combination of the radial-basis function (RBF) kernel and the white kernel is adopted. Measurements with lower SNR ($1 < \text{SNR} < 2$) are also included in the fitting to better model the decline in both bands $\gtrsim 30$ days after the peak. All three DDet candidates

² <https://www.not.iac.es/instruments/alfosc/>

³ See <https://github.com/astrocatalogs/supernovae>.

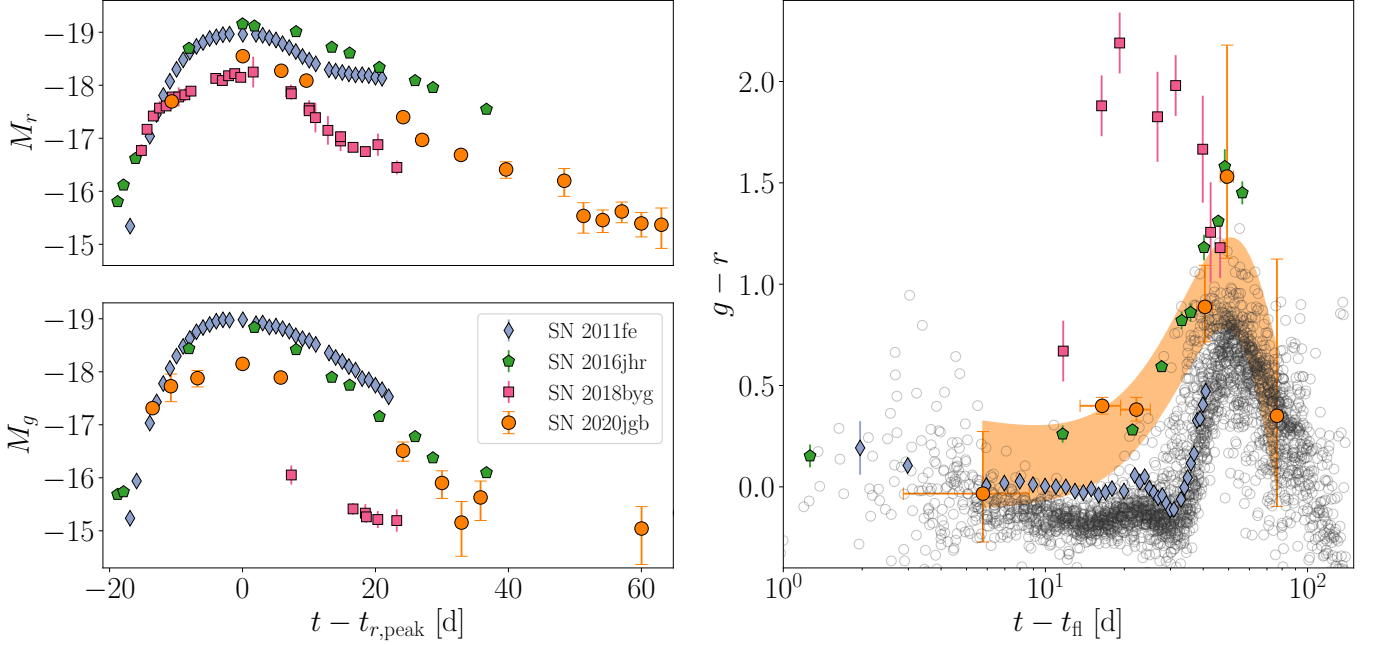


Figure 1. *Left:* Comparison of the multi-color light curves of SN 2020jgb with the normal SNe Ia SN 2011fe and the He DDet candidate SN 2018byg. The upper (lower) panel shows the evolution in g -band (r -band) absolute magnitudes. *Right:* comparison of $g - r$ color evolution to SN 2011fe and SN 2018byg, as well as 62 normal SNe Ia (open circles) with prompt observations within 5 days of first light by ZTF (Bulla et al. 2020). The shaded region denotes the 1- σ credible interval of the color of SN 2020jgb until ~ 40 days after the peak, estimated using Gaussian process.

are undoubtedly redder than normal SNe Ia. At peak light, SN 2020jgb was not as red as the extreme case, SN 2018byg ($g_{ZTF} - r_{ZTF} \approx 2.2$), but exhibited a similar color evolution as SN 2016jhr ($g - r \approx 0.5$).

3.2. Optical Spectral properties

In Figure 2, we show the optical spectral sequence of SN 2020jgb, and compare its spectra with some other SNe Ia near peak luminosity. For the spectra obtained after $+100$ d there is clear contamination from the host-galaxy, including the presence of narrow emission lines. For these spectra we have subtract the galaxy light as measured in the DEIMOS spectrum from 2022 (see Section 2.3). The earliest spectrum was obtained by SEDM ≈ 10 days before the r_{ZTF} -band peak. We only show portions of the spectrum where the $\text{SNR} > 2.5$, where the continuum is almost featureless with some marginal detection of the Si II $\lambda 6355$ at $\approx 6100 \text{ \AA}$, the trademark of SNe Ia. In subsequent spectra the Si II features become more prominent and are clearly detected through $+12$ d. To get the expansion velocity, following Maguire et al. (2014), we fit the Si II feature with a Gaussian profile. We first select the absorption region by visual inspection. The continuum is assumed to be linear. The continuum flux density at blue and red edges are also set to be free parameters, whose priors are Gaussian distributions, where the means are the flux density mea-

sured at each edge and the standard deviations are the corresponding flux uncertainties. The absorption feature is then normalized by the continuum and fit to a single Gaussian profile with three parameters (amplitude, mean velocity, velocity dispersion). Posteriors of these five parameters are sampled with emcee (Foreman-Mackey et al. 2013) using the Markov chain Monte Carlo (MCMC) method. We estimated the mean expansion velocity to be $\approx 11,500 \text{ km s}^{-1}$ near peak light.

In many SNe Ia, the spectral absorption features by Ca II infrared triplet (IRT) have two distinct components, namely the photospheric-velocity features (PVFs) and high-velocity features (HVs). The PVFs originate from the main line-forming region with typical photospheric (i.e., bulk ejecta) velocities, while the HVs are blueshifted to much shorter wavelengths, indicating significantly higher (by greater than $\sim 6000 \text{ km s}^{-1}$) velocities than typical PVFs (Silverman et al. 2015). SN 2020jgb has prominent HVs of Ca II IRT. In the earliest spectrum, the wide HVs at about $7800\text{--}8200 \text{ \AA}$ already become visible. Using the similar technique in modeling the Si II features, we fit the HVs with multiple Gaussian profiles assuming each line in the triplet can be approximated by the same profile (i.e., same amplitude and velocity dispersion), and obtained a best-fit expansion velocity $\gtrsim 26,000 \text{ km s}^{-1}$. Such HVs remain visible for over 40 days. The PVFs for Ca II IRT at about

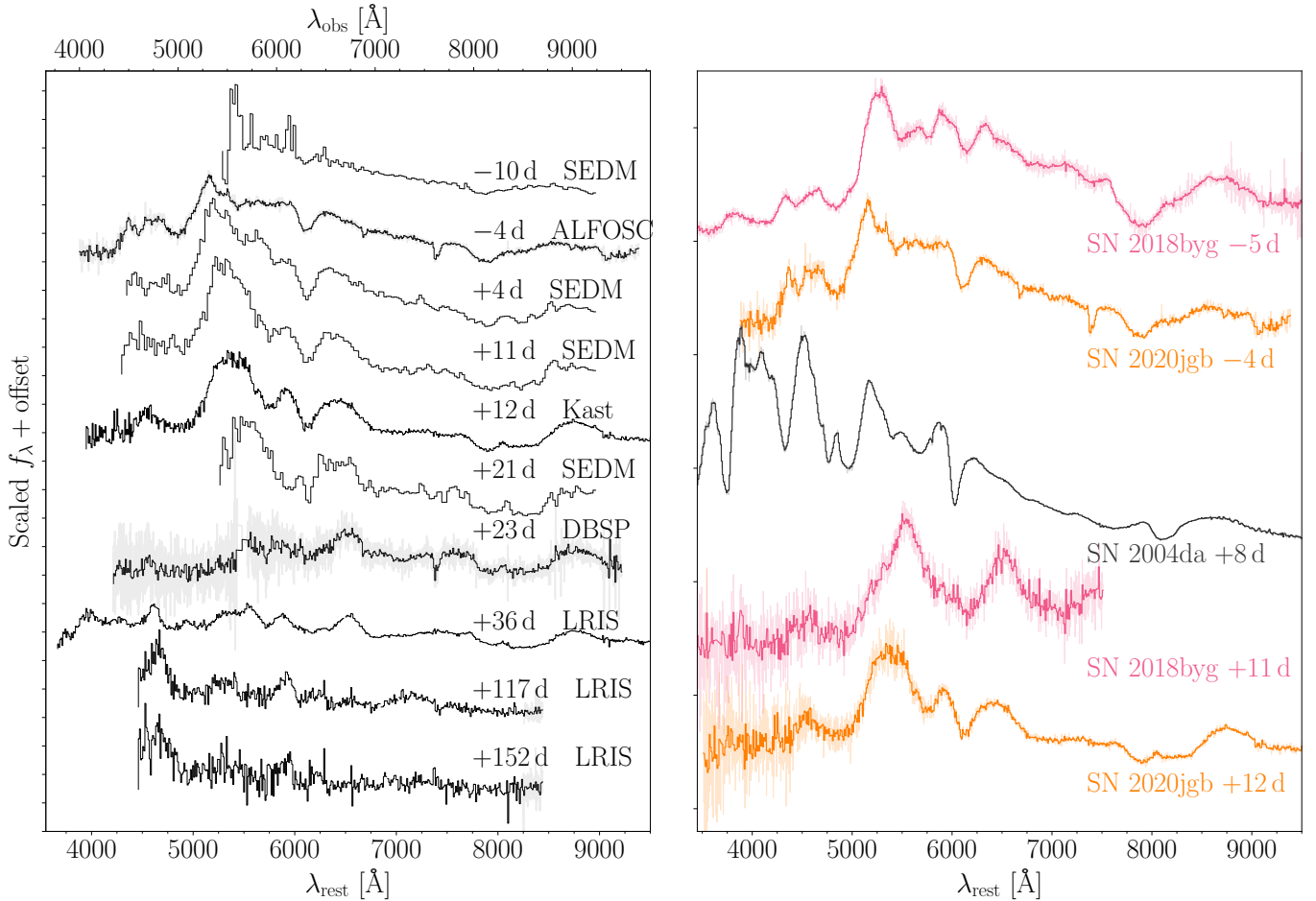


Figure 2. *Left:* optical spectral sequence of SN 2020jgb. Rest frame phases (days) relative to the r_{ZTF} -band peak and instruments used are posted next to each spectrum. The spectra are after Galactic extinction correction are shown in grey. The black lines are binned spectra with a bin size of 10 \AA , except for the SEDM spectra, whose resolution is lower than the bin size. In the last two spectra, we have subtracted the light from the host galaxy. Only regions with $\text{SNR} > 2.5$ after binning are plotted. *Right:* spectral comparison with SN 2018byg (sub-luminous He-shell DDet) and SN 2004da (normal luminosity).

$8200\text{--}8600 \text{ \AA}$ is not visible until in our second spectrum ≈ 4 days before peak light. Since then we fit the broad absorption features with two different velocity components simultaneously. The velocity of HVFs slightly declines but stays above $\approx 24,000 \text{ km s}^{-1}$, and the velocity of PVFs declines from $\approx 11,000 \text{ km s}^{-1}$ to $\approx 9,000 \text{ km s}^{-1}$. As in normal SNe Ia, the relative strength between HVFs and PVFs decreases with time.

The nebular phase spectra of SN 2020jgb are dominated by the Fe-group elements, showing some enhancement in flux between ≈ 4500 and $\approx 6000 \text{ \AA}$. We did not detect any emission feature related to $[\text{Ca II}] \lambda\lambda 7291, 7324$, which is a hallmark for Calcium-rich gap transients and is also prominent in a few DDet candidates (e.g., SN 2016hmk and SN 2019ofm; De et al. 2020).

The spectral evolution of SN 2020jgb in the optical strongly resembles SN 2018byg, a sub-luminous DDet candidate with a potentially thick helium shell. At early

times, both SNe were relatively blue and featureless with broad and shallow Ca II IRT absorption. As they evolved closer to maximum light, they developed strong continuous absorption blueward of $\approx 5000 \text{ \AA}$, while the Si II $\lambda 6355$ and the Ca II IRT became more prominent. S II was not detected in either object. In the DDet scenario, a large amount of Fe-group elements will be synthesized in the outer regions of the ejecta, which will cause significant line-blanketing near peak light (Kromer et al. 2010; Polin et al. 2019), and also high velocity intermediate-mass elements like Ca II (Fink et al. 2010; Kromer et al. 2010). This makes SN 2020jgb another promising candidate for DDet SN with a thick helium shell.

SN 2004da is a normal SNIa that shows similarities to SN 2020jgb in the NIR (Section 3.3), however, the two SNe are extremely different in the optical approximately 10 d after maximum light (Figure 2). From this

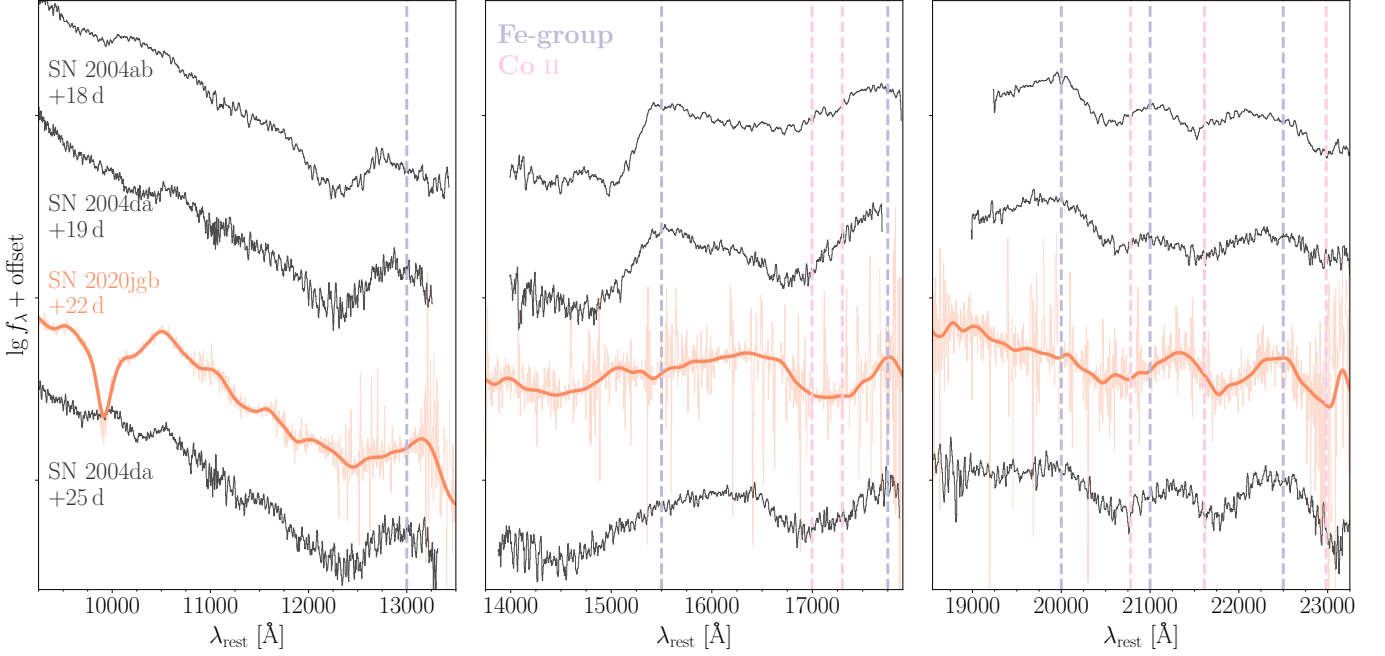


Figure 3. The NIR spectra of SN 2020jgb and two SNe Ia with normal maximum luminosity (SN 2004ab and SN 2004da, Marion et al. 2009), taken about three weeks after the peak. For each spectrum, the continuum at $\gtrsim 1.2 \mu\text{m}$ is significantly reshaped by the Fe-group blanketing (emission features, blue vertical lines) and Co II absorption (pink vertical lines).

comparison it is clear that SN 2020jgb is not a normal SNe Ia.

3.3. NIR Spectral properties

The NIR spectrum of SN 2020jgb is compared with two normal SNe Ia at a similar phase in Figure 3 (data for SNe 2004ab and 2004da from Marion et al. 2009). SN 2020jgb shows a strong absorption feature at $\sim 0.99 \mu\text{m}$, which is not seen in normal SNe Ia. This feature was still significant two weeks later, as detected by LRIS on Keck (see Figure 4), though it was only partially covered. In general, SN 2020jgb highly resembles normal SNe Ia in NIR band. The shape of the continuum redwards to $\approx 1.2 \mu\text{m}$ is significantly altered by line-blanketing of Fe-group elements synthesized in the SN interior, as opposed to the Fe-group elements in the outermost region as ashes of shell helium burning. Just like normal SNe Ia, SN 2020jgb shows an enhancement of flux at about 1.3, 1.55, 2.0, 2.1, and $2.25 \mu\text{m}$, accompanied by several Co II absorption lines. It is especially similar to SN 2004da at +25 days after maximum as the steep increase in flux at $\approx 1.55 \mu\text{m}$, known as the *H*-band break (Hsiao et al. 2019), has become less prominent.

What is not seen in usual SNe Ia is the wide, deep absorption at $\sim 0.99 \mu\text{m}$ (hereafter the $1 \mu\text{m}$ feature), indicating its peculiarity. According to Marion et al. (2009), normal SNe Ia are nearly featureless in spectra around $1 \mu\text{m}$ a few weeks after maximum light. There are several elements that may be associated with this feature,

however, none of them provide a fully satisfying explanation. Below, we discuss the origin of the peculiar $1 \mu\text{m}$ feature.

The most tantalizing possibility is that the absorption is due to He I $\lambda 1.0830 \mu\text{m}$. If SN 2020jgb is a DDet SN, then unburned He could lead to observed absorption in the spectrum, as shown in the sub-Chandrasekhar-mass He-shell DDet models of (Boyle et al. 2017). Figure 4 shows that the $1 \mu\text{m}$ feature, if associated with He I $\lambda 1.0830 \mu\text{m}$, has a high velocity ($\sim 26,000 \text{ km s}^{-1}$), especially considering the phase of the SN. The Ca II IRT also exhibits similarly high velocities at the same phase ($\sim 24,000 \text{ km s}^{-1}$), meaning it is possible to see absorption at such velocities well after maximum light. The expansion velocity in the ejecta is roughly linearly proportional to the radius, so such a high velocity indicates that both the Ca II IRT and the tentative He I absorption line form far outside the normal photosphere, which has a velocity of only $\approx 10,000 \text{ km s}^{-1}$. In the sense, the He-shell DDet scenario, in which the unburnt helium locates at the outermost ejecta, is indeed supported.

Still, this helium detection remains skeptical, since other He I are not unambiguously detected, such as the He I $\lambda 2.0581 \mu\text{m}$. Considering a line velocity of $\approx 26,000 \text{ km s}^{-1}$ and a host galaxy redshift of 0.0307, this line will be blueshifted to $\approx 1.95 \mu\text{m}$ in the observer frame, so will be strongly blended by the strong telluric lines within $1.8\text{--}2.0 \mu\text{m}$. After telluric correction, the signal to noise ratio reaches ~ 5 , with which we still cannot

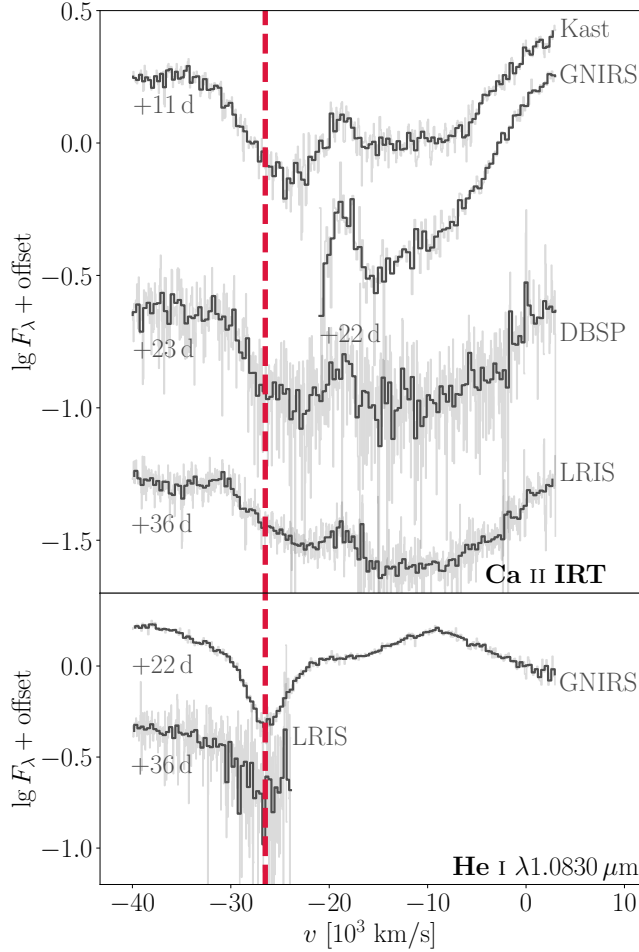


Figure 4. Spectra in the velocity space, comparing the high-velocity component of Ca II IRT and the absorption feature at $\approx 0.99 \mu\text{m}$ assuming it is associated with He I at $1.0830 \mu\text{m}$.

see any significant absorption feature. An upper limit of the equivalent width is determined to be $< 2\%$ of the $1.0830 \mu\text{m}$ line, while theoretically, the $2.0581 \mu\text{m}$ line is supposed to be only a factor of 6-12 weaker, depending on temperature (Marion et al. 2009). Another fact is that the $1 \mu\text{m}$ feature is as strong as the He I $1.0830 \mu\text{m}$ in many helium-rich core-collapse supernovae, say, Type Ib supernovae, in which the He I $2.0581 \mu\text{m}$ is weaker than the $1.0830 \mu\text{m}$ line yet still prominent (Shahbadeh et al. 2022). If the $1 \mu\text{m}$ feature is associated with He I, it would be very unusual if the $2 \mu\text{m}$ feature is not seen at all, even if somehow blended by the telluric lines. [Chang: There should be a note here about the strength of the lines in the Boyle paper... for one of their models there is no obvious 2 micron absorption] [AAM: that model is for ‘normal’ SNe Ia]

Other possibilities include the Mg II $1.0927 \mu\text{m}$, the C I $1.0693 \mu\text{m}$, and the Fe II $1.0500 \mu\text{m}$ & $1.0863 \mu\text{m}$. The Mg II $1.0927 \mu\text{m}$ line is prevalent in the NIR spec-

tra of SNe Ia, but usually disappears within a week after the peak luminosity (Marion et al. 2009), while the $1 \mu\text{m}$ feature was still visible over a month after the peak in the Keck LRIS spectrum. The required radial velocity is $\approx 30,000 \text{ km s}^{-1}$, $\approx 20\%$ faster than the HVFs of Ca II IRT at the same phase. While such a high velocity for Mg II has never been seen in other SNe Ia, since high-velocity intermediate-mass elements like magnesium and calcium can be synthesized by the detonation of helium shell (Shen & Moore 2014), the Mg II origin of the $1 \mu\text{m}$ feature cannot be strictly ruled out. But if we attribute this $1 \mu\text{m}$ feature to high-velocity Mg II, we would expect an even stronger $0.9227 \mu\text{m}$ line to be blueshifted to the red edge of the Ca II IRT, which is not detected. Given the strength of the $1 \mu\text{m}$ feature, the $0.9227 \mu\text{m}$ line should not be completely obscured by the Ca II IRT features.

The C I $1.0693 \mu\text{m}$ line from the unburnt carbon is much less frequently seen than the Mg II $1.0927 \mu\text{m}$. Hsiao et al. (2019) presented a sample of five SNe Ia with C I detections, showing the C I feature is strongest for those fainter, fast-declining objects. However, in their sample, the C I feature is a pre-maximum feature which fades away as the luminosity peaks, so the discrepancy in phase is large. The required expansion velocity $\approx 22,000 \text{ km s}^{-1}$, which is overwhelmingly faster than the estimated carbon velocity for the sample in Hsiao et al. (2019) ($\sim 10,000\text{--}12,000 \text{ km s}^{-1}$), but still consistent with the HVFs of Ca II IRT. Nonetheless, no significant carbon absorption is detected in the optical band.

The Fe II features in SNe Ia usually start to develop roughly three weeks after the peak, which is about the same phase as we obtained our GNIRS spectrum. Two Fe II lines, $0.9998 \mu\text{m}$ and $1.0500 \mu\text{m}$, are actually visible on the blue/red wings of the $1 \mu\text{m}$ feature. The Fe II $1.0863 \mu\text{m}$ line is not yet seen in the GNIRS spectrum. They correspond to an expansion velocity of $\approx 8,000 \text{ km s}^{-1}$, which is consistent with the PVFs of the Ca II IRT at the same epoch. They also match the same two lines for normal SNe Ia (Marion et al. 2009), making the identification more reliable. Obviously, these two Fe II features are wider and shallower than the strong feature between them. We fit the $1 \mu\text{m}$ feature with three Gaussian profiles. Two of them are set to be the blueshifted Fe II $0.9998 \mu\text{m}$ and $1.0500 \mu\text{m}$, and the other is an uncorrelated Gaussian profile which mainly describes the absorption in the center. We find that the shallower and wider Fe II lines only make up $\sim 40\%$ of the total equivalent width, and the rest $\sim 60\%$ comes from the central feature, which cannot be accounted for by any Fe II feature at the same velocity. Given the similarity of the Fe-group line-blanketing between the

GNIRS spectrum with the spectrum of SN 2004da at +25 days, the distribution of Fe-group elements inside each supernova ejecta should be somehow similar as normal SNe Ia, so the central region of the $1\mu\text{m}$ feature is not likely to be associated with Fe II either.

While the nature of the $1\mu\text{m}$ feature remains uncertain, other He-shell DDet candidates also seem to show similar complexity in this region. In the currently small sample of six candidates, three objects (SN 2016jhr, SN 2018aoz, and SN 2019ofm) do not have any available NIR spectra, while the other three (at quite different phases though) all exhibit strong absorption features near $1\mu\text{m}$, as shown in Figure 5. The $1\mu\text{m}$ feature for SN 2016hnk lies at a longer wavelength than SN 2020jgb, which corresponds to a lower expansion velocity, assuming they all have the same origin. The line velocity assuming a He I $\lambda 1.0830\mu\text{m}$ origin is $\approx 21,000\text{ km s}^{-1}$, which, just like SN 2020jgb, is about the same as the HVFs of the Ca II IRT in the optical spectra. The PVFs of the Ca II IRT ($\approx 10,000\text{ km s}^{-1}$) is not significantly slower than that in SN 2020jgb. For SN 2018byg, the velocity of the $1\mu\text{m}$ feature with respect to the He I $\lambda 1.0830\mu\text{m}$ is still consistent with the HVFs of Ca II IRT. But given its exotic width and lower signal-to-noise ratio, the exact line velocity is hard to determine. It is highly likely to be a mixture of several different lines.

Unfortunately, the NIR spectra for both SN 2016hnk and SN 2018byg do not cover the $2\mu\text{m}$ region, thus it is not possible to identify the presence of helium decisively. But if the $1\mu\text{m}$ feature of these objects are of the same origin, they are more likely to be correlated with the high velocity ejecta lying in the outmost region in the supernovae, because at least for SN 2020jgb and SN 2016hnk, the difference in their photospheric velocities cannot explain their discrepancy in the line velocities of the $1\mu\text{m}$ feature. Then helium is still a promising candidate to cause strong absorption near $1\mu\text{m}$ for these sub-luminous He-shell DDet SNe Ia.

Alternatively, since the NIR spectra for the three objects were all obtained at different epochs, each $1\mu\text{m}$ feature can be of completely unrelated origin. This is to be confirmed in a more complete NIR spectral sequence in future He-shell DDet SNe Ia. Even so, the seemingly ubiquitous $1\mu\text{m}$ feature in various phases is possibly a distinctive attribute against normal SNe Ia.

4. HOST GALAXY

We obtained a DEIMOS spectrum of the host galaxy, PSO J175312.663+005122.078, on 2022 March 31. The host exhibits strong, narrow emission lines including H α , H β , [N II] $\lambda 6583$, [O III] $\lambda 5007$, and [S II] $\lambda 6716$ & $\lambda 6731$. By fitting all these emission features with

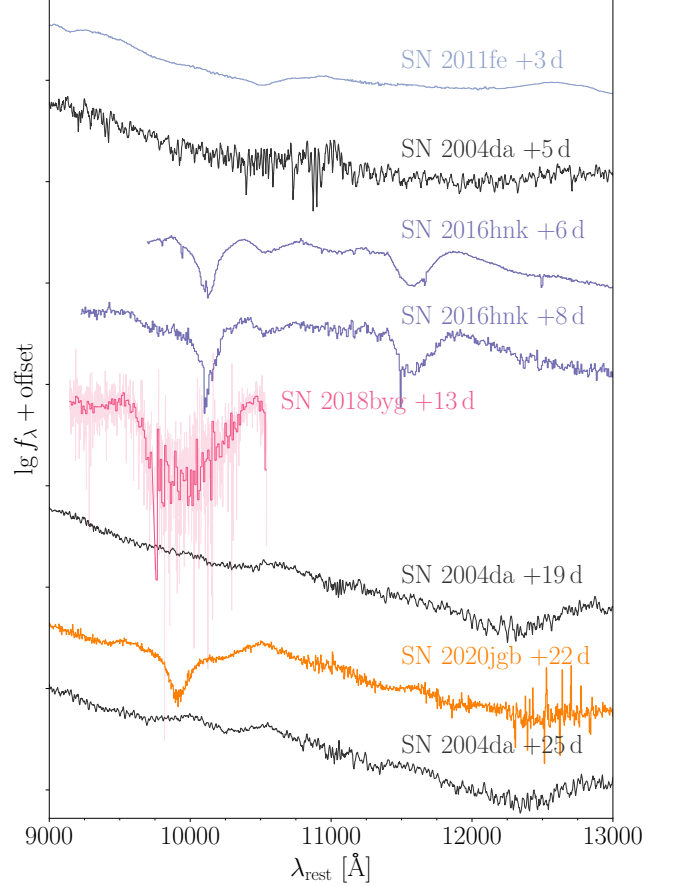


Figure 5. The NIR spectra (9,000 to 13,000 Å) of a few normal SNe Ia (SN 2011fe and SN 2004da) and three He-shell DDet candidates, which are all sub-luminous SNe Ia (SN 2016hnk, SN 2018byg, and this source, SN 2020jgb). Spectra for SN 2004da were obtained from [Marion et al. \(2009\)](#), and other spectroscopic data were obtained from the WISEREP repository ([Yaron & Gal-Yam 2012](#)).

Gaussian profiles we obtain an average redshift of $z = 0.0309 \pm 0.0003$. With the diagnostic emission line equivalent width ratios ($\log [\text{N II}]/\text{H}\alpha = -1.19 \pm 0.07$ and $\log [\text{O III}]/\text{H}\beta = 0.53 \pm 0.06$), the host is consistent with star-forming galaxies in the BPT diagram ([Baldwin et al. 1981](#); [Veilleux & Osterbrock 1987](#)).

We model the detailed properties of the host galaxy using *Prospector* ([Johnson et al. 2021](#)), a package for principled inference of stellar population properties using photometric and/or spectroscopic data. The input data included the Galactic extinction corrected DEIMOS spectrum, as well as the archival photometric data from the Panoramic Survey Telescope and Rapid Response System (Pan-STARRS; [Chambers et al. 2016](#), r , i , z Kron magnitudes) and the VISTA Hemisphere Survey (VHS; [McMahon et al. 2013](#), J and K_s Petrosian magnitudes). In the best fit, the estimated stel-

lar mass is $\log(M_* [M_\odot]) = 7.79^{+0.07}_{-0.06}$, and the specific star-formation rate (sSFR) is $\log(\text{sSFR} [\text{yr}^{-1}]) = -10.25^{+0.09}_{-0.08}$, with the uncertainties denoting the 68% credible regions.

In Figure 4, we show the sSFR and the stellar mass for the host galaxies of some He-shell DDet candidates. The host stellar properties for all four candidates are fit using **Prospector** with optical spectra from the Sloan Digital Sky Survey (SDSS; York et al. 2000) and photometry from the DESI Legacy Imaging Surveys (Dey et al. 2019, g , r , z , W_1 , W_2 magnitudes). With mid-infrared photometry available, **prospector** can better estimate the overall dust extinction in the host galaxy and the contribution of an active galactic nucleus (AGN) to the spectral energy distribution (SED). When fitting the SEDs of these hosts, we found for the two nearby ($z \lesssim 0.03$) late-type hosts of SN 2016hmk and SN 2019ofm, both surveys only cover their bright bulges where the star-formation has almost quenched, leaving out their blue, extended spiral structures where there is still ongoing star-formation. Hence only the bulge properties are modeled. While the estimated stellar mass should represent the total stellar mass well, the best-fit SFR is a poor estimator for the total SFR. Therefore, for the host of SN 2016hmk, we adopted the results in Galbany et al. (2019) as part of the PMAS/PPak Integral-field Supernova Hosts Compilation (PISCO; Galbany et al. 2018), where the photons from the H II regions in the spiral arms were also collected using integral field spectroscopy. For the host of SN 2019ofm, we do not have any available integral field spectroscopic data, so we still show our best-fit stellar mass and sSFR in Figure 4, where the sSFR should be regarded as a lower limit. The host of SN 2018aoz (NGC 3923) is a very nearby ($z = 0.00580$) early-type galaxy and is outside the footprint of SDSS, so we adopt its stellar population properties from the Census of the Local Universe (CLU) catalog [AAM: References?].

Given the limited sample size yet, the host environments of the He-shell DDet candidates have started to show diversity. Among the six objects we have, SN 2018byg and SN 2018aoz resided in older stellar populations, while other candidates emerged in younger, star-forming regions. This is true for both thin shell objects of normal luminosity (SN 2016jhr in a star-forming host, SN 2018aoz in a quenched host) and thick shell, sub-luminous objects (SN 2020jgb in a star-forming host, SN 2018byg in a quenched host), even when the natures of SN 2016hmk and SN 2019ofm remain ambiguous. In this sense, the He-shell DDet sample resembles the SNe Ia population in general, which can occur in both star-forming and quenched galaxies, with tentative prefer-

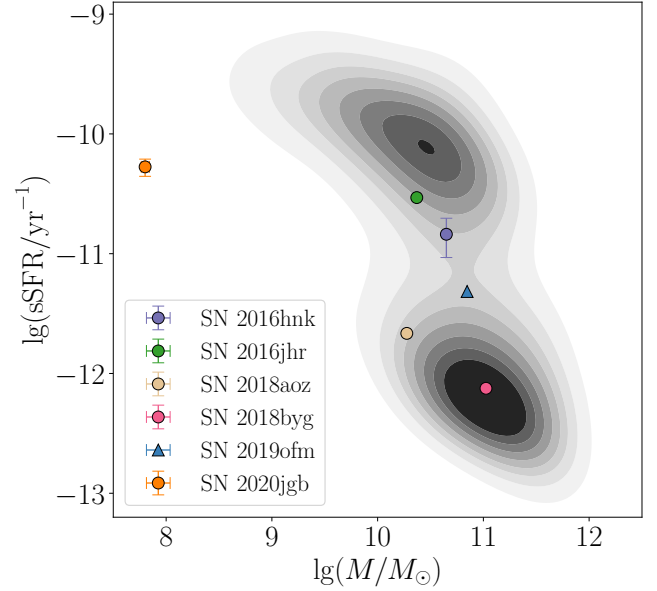


Figure 6. The specific star-formation rate (sSFR) and the stellar mass for the host galaxies of He-shell DDet candidates. The properties for the hosts of SN 2016hmk and SN 2018aoz are taken from Galbany et al. (2019) and the CLU catalog [AAM: References?], respectively. For the sSFR in the host of SN 2019ofm, only a lower limit is shown (the triangle). The background is a sample of galaxies from the SDSS MPA-JHU DR8 catalog (Kauffmann et al. 2003; Brinchmann et al. 2004). Galaxies with BPT classification as AGNs or LINERs are excluded, since certain spectral features (e.g., H α emission) due to nuclear activities might be misinterpreted as star formation.

ence to the host environment with a higher sSFR (e.g., Sullivan et al. 2006; Smith et al. 2012). But such a diversity in host environments is very different from some other types thermonuclear supernovae, such as type-Iax supernovae (SNe Iax) which almost only appear in star-forming galaxies, or SN 1991bg-like and SN 2002es-like objects, which strongly prefer old stellar environments (see the review in Jha et al. 2019).

Talk about de los Reyes et al. (2020). [AAM: de los Reyes et al. (2020) suggest that sub-Chandrasekhar SNe Ia have a shorter delay timescale than near-Chandrasekhar SNe Ia or SNe Iax. This is not immediately related to the current star-formation at the explosion sites, though there should be a stronger preference towards younger stellar populations than near-Chandrasekhar SNe Ia.]

5. MODEL COMPARISONS

A few sentences from Abi describing the models.

In Figure 5, we show the comparison of the photometric and spectroscopic features of SN 2020jgb with

DDet models from Polin et al. (2019). The peak luminosity reflects the total progenitor mass (C/O core + He shell), and we find models with a total mass of $0.95 M_{\odot}$ generally reproduce the r -band peak brightness well. Thus in Figure 5, the total mass is fixed to be $0.95 M_{\odot}$ in all models. The overall r -band photometric evolution is best fit by the model with a $0.87 M_{\odot}$ C/O core and a $0.08 M_{\odot}$ He shell, while all three models underestimate the g -band brightness after the peak. This deviation may be attributed to a variety of factors on handling the explosion and radiative transfer. First, throughout the simulations we assume local thermodynamic equilibrium (LTE), which is not valid once the ejecta becomes optically thin. Typically the bulk ejecta of a sub-Chandrasekhar SNe Ia remains optically thick for ~ 30 days since the explosion. But in modeling the brightness g -band, the LTE assumption is even more tricky, because the major opacity in g -band comes from the Fe-group line-blanketing in the outermost ejecta, where the optical depth may evolve differently from that at the photosphere. Hence the LTE condition may quickly become inapplicable. Furthermore, our 1D He shell model is not capable to capture the multi-dimensional effects in the explosion such as

asymmetries. In previous studies on other DDet objects, the g -band brightness is systematically under-predicted shortly after the peak, despite the fact that redder bands can be fit decently (e.g. Jiang et al. 2017; Jacobson-Galán et al. 2020).

The model which best fits the photometry ($0.87 M_{\odot} + 0.08 M_{\odot}$) also reproduces the major absorption features (e.g., Fe-group line-blanketing, Si II $\lambda 6355$, Ca II IRT) and the corresponding expansion velocities near the peak light. The discrepancies include underestimating the strength of the HVFs of Ca II IRT and the flux bump at $\approx 5000 \text{ \AA}$ and overestimating the continuum flux in the near infrared. In addition, the predicted Si II $\lambda 5972$ does not show up in the NOT spectrum.

Conclusions from the model comparison.

6. DISCUSSION AND CONCLUSION

Facility:

Software: `astropy` (Astropy Collaboration et al. 2013), `emcee` (Foreman-Mackey et al. 2013), `matplotlib` (Hunter 2007), `prospector` (Johnson et al. 2022), `PyPeIt` (Prochaska et al. 2020), `scikit-learn` (Pedregosa et al. 2011), `scipy` (Virtanen et al. 2020), ...

REFERENCES

- Astropy Collaboration, Robitaille, T. P., Tollerud, E. J., et al. 2013, *A&A*, 558, A33, doi: [10.1051/0004-6361/201322068](https://doi.org/10.1051/0004-6361/201322068)
- Baldwin, J. A., Phillips, M. M., & Terlevich, R. 1981, *PASP*, 93, 5, doi: [10.1086/130766](https://doi.org/10.1086/130766)
- Bellm, E. C., Kulkarni, S. R., Graham, M. J., et al. 2019, *PASP*, 131, 018002, doi: [10.1088/1538-3873/aaecbe](https://doi.org/10.1088/1538-3873/aaecbe)
- Blagorodnova, N., Neill, J. D., Walters, R., et al. 2018, *PASP*, 130, 035003, doi: [10.1088/1538-3873/aaa53f](https://doi.org/10.1088/1538-3873/aaa53f)
- Boyle, A., Sim, S. A., Hachinger, S., & Kerzendorf, W. 2017, *A&A*, 599, A46, doi: [10.1051/0004-6361/201629712](https://doi.org/10.1051/0004-6361/201629712)
- Brinchmann, J., Charlot, S., White, S. D. M., et al. 2004, *MNRAS*, 351, 1151, doi: [10.1111/j.1365-2966.2004.07881.x](https://doi.org/10.1111/j.1365-2966.2004.07881.x)
- Bulla, M., Miller, A. A., Yao, Y., et al. 2020, *ApJ*, 902, 48, doi: [10.3847/1538-4357/abb13c](https://doi.org/10.3847/1538-4357/abb13c)
- Carrick, J., Turnbull, S. J., Lavaux, G., & Hudson, M. J. 2015, *MNRAS*, 450, 317, doi: [10.1093/mnras/stv547](https://doi.org/10.1093/mnras/stv547)
- Cenko, S. B., Fox, D. B., Moon, D.-S., et al. 2006, *PASP*, 118, 1396, doi: [10.1086/508366](https://doi.org/10.1086/508366)
- Chambers, K. C., Magnier, E. A., Metcalfe, N., et al. 2016, *arXiv e-prints*, arXiv:1612.05560, <https://arxiv.org/abs/1612.05560>
- Dahiwal, A., & Fremling, C. 2020, *Transient Name Server Classification Report*, 2020-1624, 1
- De, K., Kasliwal, M. M., Polin, A., et al. 2019, *The Astrophysical Journal*, 873, L18, doi: [10.3847/2041-8213/ab0aec](https://doi.org/10.3847/2041-8213/ab0aec)
- De, K., Kasliwal, M. M., Tzanidakis, A., et al. 2020, *The Astrophysical Journal*, 905, 58, doi: [10.3847/1538-4357/abb45c](https://doi.org/10.3847/1538-4357/abb45c)
- De, K., Kasliwal, M. M., Tzanidakis, A., et al. 2020, *ApJ*, 905, 58, doi: [10.3847/1538-4357/abb45c](https://doi.org/10.3847/1538-4357/abb45c)
- de los Reyes, M. A. C., Kirby, E. N., Seitzenzahl, I. R., & Shen, K. J. 2020, *ApJ*, 891, 85, doi: [10.3847/1538-4357/ab736f](https://doi.org/10.3847/1538-4357/ab736f)
- Dey, A., Schlegel, D. J., Lang, D., et al. 2019, *AJ*, 157, 168, doi: [10.3847/1538-3881/ab089d](https://doi.org/10.3847/1538-3881/ab089d)
- Duev, D. A., Mahabal, A., Masci, F. J., et al. 2019, *MNRAS*, 489, 3582, doi: [10.1093/mnras/stz2357](https://doi.org/10.1093/mnras/stz2357)
- Elias, J. H., Vukobratovich, D., Andrew, J. R., et al. 1998, in *Society of Photo-Optical Instrumentation Engineers (SPIE) Conference Series*, Vol. 3354, *Infrared Astronomical Instrumentation*, ed. A. M. Fowler, 555–565, doi: [10.1117/12.317281](https://doi.org/10.1117/12.317281)

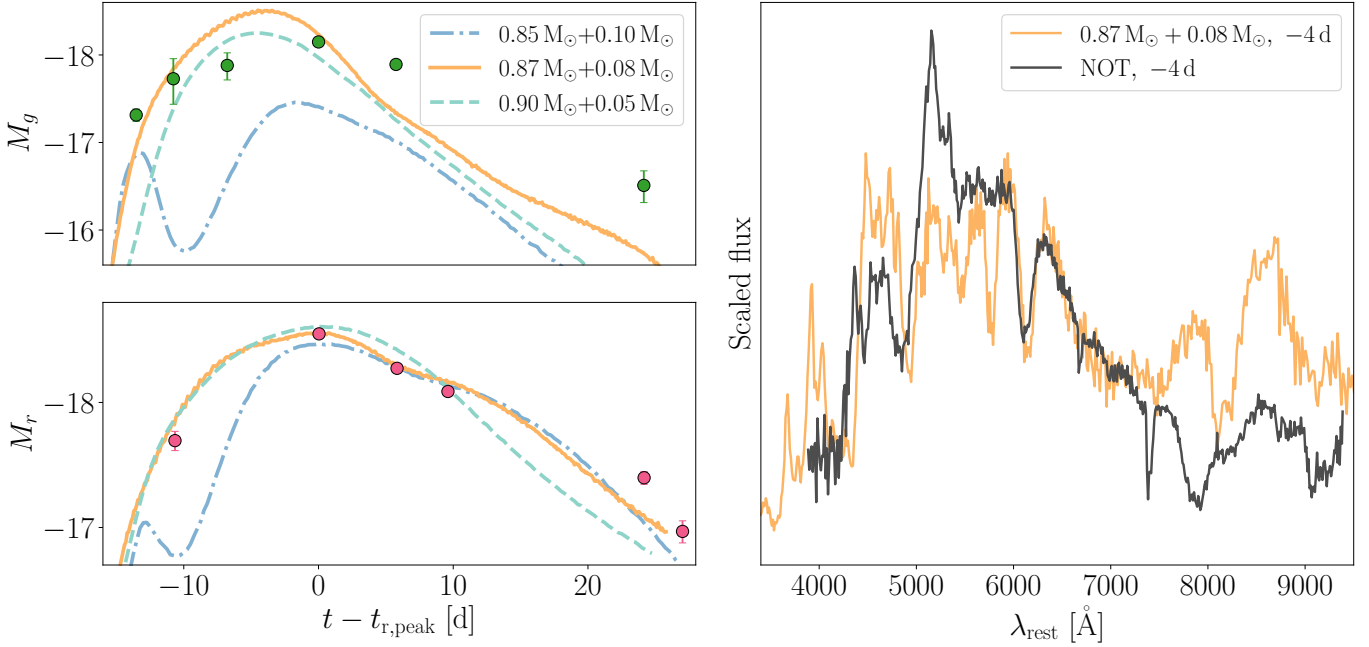


Figure 7. *Left:* Comparison of the photometric evolution of SN 2020jgb with the He-shell DDet models from Polin et al. (2019). The model parameters are indicated in the legend as (C/O core mass + He shell mass). The upper (lower) panel shows the evolution in g -band (r -band) absolute magnitudes. *Right:* Comparison of the spectrum of SN 2020jgb with the $0.87 M_{\odot}$ C/O core + $0.08 M_{\odot}$ He shell DDet model before peak luminosity. Each spectrum is normalized by the median flux between 6500 and 7500 Å, and binned with a size of 10 Å. The synthetic spectrum 4 days before the r -band peak best matches the NOT spectrum (Galactic extinction corrected), which was obtained ~ 4 days before the r_{ZTF} -band peak. All the phases have been rescaled to the host galaxy rest frame.

Faber, S. M., Phillips, A. C., Kibrick, R. I., et al. 2003, in Society of Photo-Optical Instrumentation Engineers (SPIE) Conference Series, Vol. 4841, Instrument Design and Performance for Optical/Infrared Ground-based Telescopes, ed. M. Iye & A. F. M. Moorwood, 1657–1669, doi: [10.1117/12.460346](https://doi.org/10.1117/12.460346)

Fink, M., Röpke, F. K., Hillebrandt, W., et al. 2010, A&A, 514, A53, doi: [10.1051/0004-6361/200913892](https://doi.org/10.1051/0004-6361/200913892)

Fitzpatrick, E. L. 1999, PASP, 111, 63, doi: [10.1086/316293](https://doi.org/10.1086/316293)

Foreman-Mackey, D., Hogg, D. W., Lang, D., & Goodman, J. 2013, PASP, 125, 306, doi: [10.1086/670067](https://doi.org/10.1086/670067)

Fremling, C. 2020, Transient Name Server Discovery Report, 2020-1247, 1

Galbany, L., Anderson, J. P., Sánchez, S. F., et al. 2018, ApJ, 855, 107, doi: [10.3847/1538-4357/aaaf20](https://doi.org/10.3847/1538-4357/aaaf20)

Galbany, L., Ashall, C., Höflich, P., et al. 2019, Astronomy & Astrophysics, 630, A76, doi: [10.1051/0004-6361/201935537](https://doi.org/10.1051/0004-6361/201935537)

Graham, M. J., Kulkarni, S. R., Bellm, E. C., et al. 2019, PASP, 131, 078001, doi: [10.1088/1538-3873/ab006c](https://doi.org/10.1088/1538-3873/ab006c)

Guillochon, J., Parrent, J., Kelley, L. Z., & Margutti, R. 2017, ApJ, 835, 64, doi: [10.3847/1538-4357/835/1/64](https://doi.org/10.3847/1538-4357/835/1/64)

Hsiao, E. Y., Phillips, M. M., Marion, G. H., et al. 2019, PASP, 131, 014002, doi: [10.1088/1538-3873/aae961](https://doi.org/10.1088/1538-3873/aae961)

Hunter, J. D. 2007, Computing in Science and Engineering, 9, 90, doi: [10.1109/MCSE.2007.55](https://doi.org/10.1109/MCSE.2007.55)

Jacobson-Galán, W. V., Polin, A., Foley, R. J., et al. 2020, The Astrophysical Journal, 896, 165, doi: [10.3847/1538-4357/ab94b8](https://doi.org/10.3847/1538-4357/ab94b8)

Jha, S. W., Maguire, K., & Sullivan, M. 2019, Nature Astronomy, 3, 706, doi: [10.1038/s41550-019-0858-0](https://doi.org/10.1038/s41550-019-0858-0)

Jiang, J.-a., Doi, M., Maeda, K., et al. 2017, Nature, 550, 80, doi: [10.1038/nature23908](https://doi.org/10.1038/nature23908)

Johnson, B., Leja, J., Bowman, W., et al. 2022, bd-j/prospector: v1.1, v1.1.0, Zenodo, doi: [10.5281/zenodo.6192136](https://doi.org/10.5281/zenodo.6192136)

Johnson, B. D., Leja, J., Conroy, C., & Speagle, J. S. 2021, ApJS, 254, 22, doi: [10.3847/1538-4365/abef67](https://doi.org/10.3847/1538-4365/abef67)

Kauffmann, G., Heckman, T. M., White, S. D. M., et al. 2003, MNRAS, 341, 33, doi: [10.1046/j.1365-8711.2003.06291.x](https://doi.org/10.1046/j.1365-8711.2003.06291.x)

Kromer, M., Sim, S. A., Fink, M., et al. 2010, ApJ, 719, 1067, doi: [10.1088/0004-637X/719/2/1067](https://doi.org/10.1088/0004-637X/719/2/1067)

Maguire, K., Sullivan, M., Pan, Y. C., et al. 2014, MNRAS, 444, 3258, doi: [10.1093/mnras/stu1607](https://doi.org/10.1093/mnras/stu1607)

- Mahabal, A., Rebbapragada, U., Walters, R., et al. 2019, *PASP*, 131, 038002, doi: [10.1088/1538-3873/aaf3fa](https://doi.org/10.1088/1538-3873/aaf3fa)
- Marion, G. H., Höflich, P., Gerardy, C. L., et al. 2009, *AJ*, 138, 727, doi: [10.1088/0004-6256/138/3/727](https://doi.org/10.1088/0004-6256/138/3/727)
- Masci, F. J., Laher, R. R., Rusholme, B., et al. 2019, *PASP*, 131, 018003, doi: [10.1088/1538-3873/aae8ac](https://doi.org/10.1088/1538-3873/aae8ac)
- Matheson, T., Filippenko, A. V., Barth, A. J., et al. 2000, *AJ*, 120, 1487, doi: [10.1086/301518](https://doi.org/10.1086/301518)
- McMahon, R. G., Banerji, M., Gonzalez, E., et al. 2013, *The Messenger*, 154, 35
- Miller, J., & Stone, R. 1994, *The Kast Double Spectrograph*, Lick Observatory technical reports (University of California Observatories/Lick Observatory).
<https://books.google.com/books?id=QXk2AQAAIAAJ>
- Ni, Y. Q., Moon, D.-S., Drout, M. R., et al. 2022, *Nature Astronomy*, doi: [10.1038/s41550-022-01603-4](https://doi.org/10.1038/s41550-022-01603-4)
- Nugent, P. E., Sullivan, M., Cenko, S. B., et al. 2011, *Nature*, 480, 344, doi: [10.1038/nature10644](https://doi.org/10.1038/nature10644)
- Oke, J. B., & Gunn, J. E. 1982, *PASP*, 94, 586, doi: [10.1086/131027](https://doi.org/10.1086/131027)
- Oke, J. B., Cohen, J. G., Carr, M., et al. 1995, *PASP*, 107, 375, doi: [10.1086/133562](https://doi.org/10.1086/133562)
- Patterson, M. T., Bellm, E. C., Rusholme, B., et al. 2019, *PASP*, 131, 018001, doi: [10.1088/1538-3873/aae904](https://doi.org/10.1088/1538-3873/aae904)
- Pedregosa, F., Varoquaux, G., Gramfort, A., et al. 2011, *Journal of Machine Learning Research*, 12, 2825
- Polin, A., Nugent, P., & Kasen, D. 2019, *ApJ*, 873, 84, doi: [10.3847/1538-4357/aafb6a](https://doi.org/10.3847/1538-4357/aafb6a)
- Poznanski, D., Ganeshalingam, M., Silverman, J. M., & Filippenko, A. V. 2011, *MNRAS*, 415, L81, doi: [10.1111/j.1745-3933.2011.01084.x](https://doi.org/10.1111/j.1745-3933.2011.01084.x)
- Prochaska, J. X., Hennawi, J. F., Westfall, K. B., et al. 2020, *Journal of Open Source Software*, 5, 2308, doi: [10.21105/joss.02308](https://doi.org/10.21105/joss.02308)
- Prochaska, J. X., Hennawi, J., Cooke, R., et al. 2020, *pypeit/PyPeIt: Release 1.0.0, v1.0.0*, Zenodo, doi: [10.5281/zenodo.3743493](https://doi.org/10.5281/zenodo.3743493)
- Schlafly, E. F., & Finkbeiner, D. P. 2011, *ApJ*, 737, 103, doi: [10.1088/0004-637X/737/2/103](https://doi.org/10.1088/0004-637X/737/2/103)
- Shahbandeh, M., Hsiao, E. Y., Ashall, C., et al. 2022, *ApJ*, 925, 175, doi: [10.3847/1538-4357/ac4030](https://doi.org/10.3847/1538-4357/ac4030)
- Shen, K. J., & Moore, K. 2014, *ApJ*, 797, 46, doi: [10.1088/0004-637X/797/1/46](https://doi.org/10.1088/0004-637X/797/1/46)
- Silverman, J. M., Vinkó, J., Marion, G. H., et al. 2015, *MNRAS*, 451, 1973, doi: [10.1093/mnras/stv1011](https://doi.org/10.1093/mnras/stv1011)
- Smith, M., Nichol, R. C., Dilday, B., et al. 2012, *ApJ*, 755, 61, doi: [10.1088/0004-637X/755/1/61](https://doi.org/10.1088/0004-637X/755/1/61)
- Sullivan, M., Le Borgne, D., Pritchett, C. J., et al. 2006, *ApJ*, 648, 868, doi: [10.1086/506137](https://doi.org/10.1086/506137)
- Veilleux, S., & Osterbrock, D. E. 1987, *ApJS*, 63, 295, doi: [10.1086/191166](https://doi.org/10.1086/191166)
- Virtanen, P., Gommers, R., Oliphant, T. E., et al. 2020, *Nature Methods*, 17, 261, doi: [10.1038/s41592-019-0686-2](https://doi.org/10.1038/s41592-019-0686-2)
- Yaron, O., & Gal-Yam, A. 2012, *PASP*, 124, 668, doi: [10.1086/666656](https://doi.org/10.1086/666656)
- York, D. G., Adelman, J., Anderson, John E., J., et al. 2000, *AJ*, 120, 1579, doi: [10.1086/301513](https://doi.org/10.1086/301513)
- Zackay, B., Ofek, E. O., & Gal-Yam, A. 2016, *ApJ*, 830, 27, doi: [10.3847/0004-637X/830/1/27](https://doi.org/10.3847/0004-637X/830/1/27)